Strain-Sensitive Flexible Magnetoelectric Ceramic Nanocomposites

Author(s):
Kim, Min-Soo; Kim, Donghoon; Aktas, Buse; Choi, Hongsoo; Puigmartí-Luis, Josep; Nelson, Bradley; Pané, Salvador; Chen, Xiang-Zhong

Publication date:
2023-03-24

Permanent link:
https://doi.org/10.3929/ethz-b-000603625

Originally published in:
Advanced Materials Technologies 8(6), https://doi.org/10.1002/admt.202202097

Funding acknowledgement:
771565C - Highly Integrated Nanoscale Robots for Targeted Delivery to the Central Nervous System (EC)
764977 - Advanced integrative solutions to Corrosion problems beyond micro-scale: towards long-term durability of miniaturized Biomedical, Electronic and Energy systems (EC)
743217 - Soft Micro Robotics (EC)
192012 - Mechano-chromic, Voltage-sensitive Electrostimulators: Innovative Piezoelectric Biomaterials for Electro-stimulated Cellular growth (SNF)
190451 - 3D Magnetic Nanoparticle Assemblies for Tumor-Targeted Nanomedicine: a Microrobotic Approach (SNF)
197017 - Flexible Electronics meets µ-Robotics: Route for Augmented Bio-Intelligent Medical Treatments (SNF)

ADVANCED MATERIALS TECHNOLOGIES
www.advmattechnol.de

Strain-Sensitive Flexible Magnetoelectric Ceramic Nanocomposites

Minsoo Kim, Donghoon Kim, Buse Aktas, Hongsoo Choi, Josep Puigmartí-Luis, Bradley J. Nelson, Salvador Pané, and Xiang-Zhong Chen**

Magnetoelectric (ME) oxide materials can convert magnetic input into electric output and vice versa, making them excellent candidates for advanced sensing, data storage, and communication. However, their application has been limited to rigid devices due to their brittle nature. Here, flexible ME oxide composite ($BaTiO_3/CoFe_2O_4$) thin film nanostructures with distinct ME coupling coefficients are reported. In contrast to rigid bulk counterparts, these ceramic nanostructures display a flexible behavior after being released from the substrate, and can be transferred onto a stretchable substrate such as polydimethylsiloxane. These ceramic films possess high ME coefficients due to minimized clamping effect and preferred crystalline orientation, and exhibit reversibly tunable ME coupling via mechanical stretching thanks to their large elasticity (>4%). It is believed that the study can open up new avenues for integrating ceramic ME composites into micro-/nanoelectromechanical system and soft robotic devices.

1. Introduction

Novel functional materials can provide innovations in soft robotics and micro-/nanoelectromechanical systems (M/NEMS) for advanced sensing, actuation, and communication applications.[1–4] While polymer-based materials are considered promising for flexible devices due to their elastic properties, their functional performance is still inferior to those of inorganic materials, such as ceramics. For example, commercially available ceramics possess piezoelectric constants that are orders of magnitude higher than those of piezoelectric polymers (e.g., $BaTiO_3$: 191 pC N^{-1} vs P(VDF-TrFE): 25–30 pC N^{-1}).[5,6] Although the rigid mechanical nature of ceramic materials has hindered their utilization in flexible devices, recent observations of abnormal mechanical properties in nanoscale ceramic materials could resolve these issues. Specifically, free-standing nanoscale oxide thin films exhibit distinguished mechanical properties such as superelasticity[7–9] and extreme tensile strain endurance,[10,11] in contrast to brittle bulk ceramics or thin films on substrates. Additionally, the free-standing thin films can be transferred onto flexible or stretchable substrates,[12–14] which highly facilitates the integration of these functional oxides into soft robotics and M/NEMS.

Functional ceramic oxides that show coupling between mechanical, electrical, and magnetic order parameters[15] are appealing for a wide range of applications. Magnetoelectric (ME) composites composed of piezoelectric and magnetostrictive oxides are a clear example of this class of materials, where the coupling is achieved through interfacial elastic interactions. As ME composite oxides can detect magnetic fields and convert them into electric outputs, they have been widely applied in smart sensors,[16,17] memories,[18,19] and biomedical systems.[20] Extending these superior ME devices to flexible systems would require strong ME coupling and excellent elastic mechanical properties. However, these highly functional ME composite oxides have not been incorporated into flexible systems due to their hard and brittle nature in bulk.

Here, we realize flexible ME composite oxides by creating $BaTiO_3/CoFe_2O_4$ (BTO/CFO) free-standing epitaxial bilayer thin films. We show these free-standing thin films have large elastic tensile strain (>4%) and can be transferred to flexible substrates, such as polydimethylsiloxane (PDMS), even with

M. Kim, D. Kim, B. Aktas, B. J. Nelson, S. Pané, X.-Z. Chen
Multi-Scale Robotics Lab
Institute of Robotics and Intelligent Systems
ETH Zurich
Tannenstrasse 3, Zurich 8092, Switzerland
E-mail: vidalp@ethz.ch; chenxian@ethz.ch

The ORCID identification number(s) for the author(s) of this article can be found under https://doi.org/10.1002/admt.202202097.

DOI: 10.1002/admt.202202097

H. Choi
Department of Robotics & Mechatronics Engineering
DGIST-ETH Microrobotics Research Center
Daegu Gyeong-buk Institute of Science and Technology (DGIST)
333 Techno Jungang-daero, Hyeonpung-Myeon, Dalseong-Gun
Daegu 42988, Republic of Korea

J. Puigmartí-Luis
Departament de Ciència dels Materials i Química Física
Institut de Química Teòrica i Computacional
University of Barcelona (UB)
Martí i Franquès, 1, 08028 Barcelona, Spain

J. Puigmartí-Luis
Institució Catalana de Recerca i Estudis Avançats (ICREA)
Pg. Lluís Companys 23, 08010 Barcelona, Spain

complex geometries. We also investigate the ME performance of these composite oxides. The free-standing and transferred BTO/CFO structures exhibit an order of magnitude larger ME coupling compared to thin films on a substrate as they are free from the substrate clamping.[21] We also investigate how applied deformations influence the ME coupling and determine the strain dependency of the ME coupling in the transferred BTO/CFO structures by stretching the PDMS substrate. Our study not only represents a strategy for implementing ME oxide ceramics in soft robotic devices and M/NEMS, but also provides insight into their performance.

2. Results and Discussion

Figure 1 shows the flexible ME composites transferred onto a PDMS substrate that can endure bending and stretching. The free-standing BTO/CFO structures were fabricated using photolithography, dry etching, and wet etching processes sequentially (Figure 1a). Different patterns were designed on the as-deposited BTO/CFO films through photolithography and Ar-ion milling. The patterned nanostructures were then released through selective etching of the underlying MgO substrate followed by critical point drying (details in Section 4). When both ends of the BTO/CFO thin film structures were fixed, then a micro "bridge" can be obtained. When only one end of the microstructure is fixed, then, after etching and release, BTO/CFO bilayer thin film will curl due to the interfacial stress brought by the lattice mismatch.[9] These curled free-standing BTO/CFO structures demonstrated flexible nature (Figure 1b, Movie S1, Supporting Information) when they were deformed by a micro tip. The deformed structures were recovered to their original shapes without permanent deformation, similar to superelasticity. The free-standing BTO/CFO micro "bridge" structures were transferred to a stretchable PDMS substrate by direct stamping. The transferred structures showed good flexibility, stretchability, and endurance to different types of deformations, for example, bending through the PDMS substrate (Figure 1c).

We quantitatively investigated the stretchability of BTO/CFO free-standing films by nanomechanical tensile test. In contrast to bulk ceramics, extreme elongations were observed in the

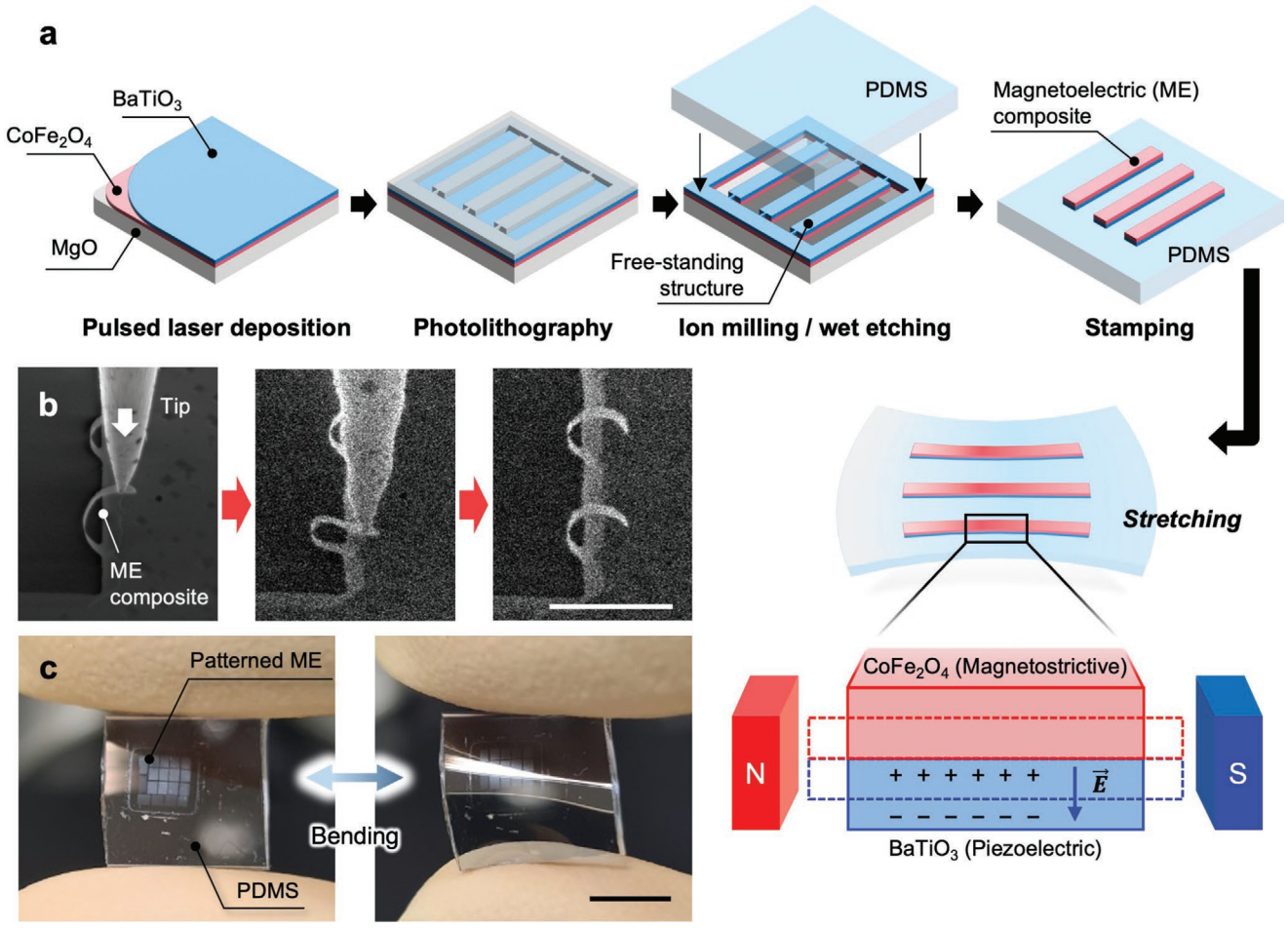

Figure 1. Flexible and stretchable magnetoelectrics. a) Schematic illustration of the fabrication processes of flexible and stretchable magnetoelectrics. Free-standing BTO/CFO structures were stamp-transferred onto the PDMS substrate. b) Bending of the curved free-standing BTO/CFO structures. A curved structure is fabricated when one end is free. The structure was recovered to the initial curve after deformation. The scale bar indicates 10 µm. c) Application of bending strains to the transferred BTO/CFO structures via PDMS substrate. The scale bar indicates 5 mm.

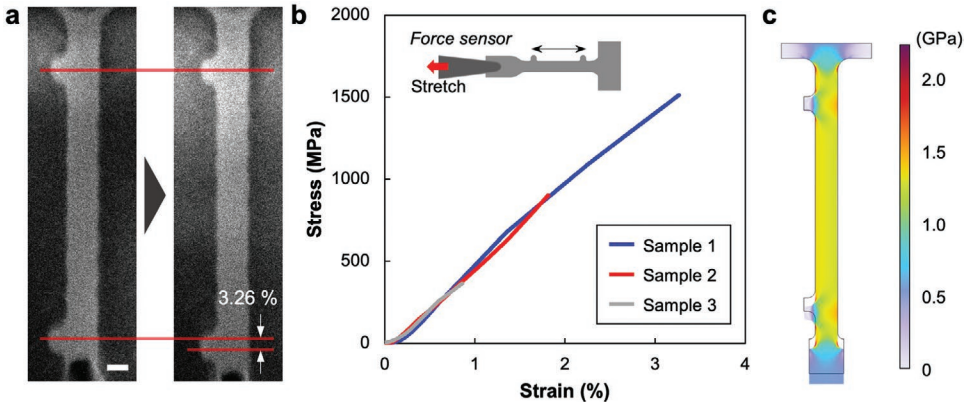

Figure 2. Mechanical tensile tests of BTO/CFO free-standing structures. a) SEM images of a dogbone-like structure during the tensile failure test. The scale bar indicates 1 µm. b) Stress–strain curves obtained during the tensile failure test and the schematic illustration of the tensile test configuration (inset). c) Finite element method-based mechanical simulations of dogbone-like structures.

dogbone-like structures (**Figure 2**a, Movie S2, Supporting Information, details in Section 4).[22] The stress–strain curve from the fracture test shows maximum failure stress and strain of 1514 MPa and 3.26% (blue, Figure 2b), respectively. The tensile strain is significantly larger than that of bulk ceramic materials. Although earlier fractures have been observed, including failure stress and strain of 0.89% and 301.2 MPa (grey) and 1.81% and 772.6 MPa (red), the slope of each stress–strain curve, namely, the Young's modulus ($E = \frac{\sigma}{\varepsilon}$) of the structure, is almost identical for all three cases with a value of 48.8 GPa (± 1.87 GPa), which indicates the reliability of the measurements and the repeatability of the performance of the material. The early fracture points can be ascribed to i) stress concentration near the markers and ii) uneven contact between the structure and the force sensor. In most cases, fractures occurred near the marker or the contact point between the sample and the force sensor (Figure S1, Supporting Information), indicating an early fracture caused by the stress concentration. Mechanical analysis using the finite-element method further corroborates the hypothesis that stress is concentrated near the marker points and the contact point (Figure 2c). While the exact strain analysis was difficult to ascertain without markers, fractures occurred in the middle of the neck in some cases (Figure S2, Supporting Information). In addition, AFM topography images (Figure S3, Supporting Information) of the stretched BTO/CFO (a tensile strain of ≈4.1%) without displaying any cracks further indicate a larger failure tensile strain in BTO/CFO free-standing structures. These enhanced fracture stress and strain values can enable ME composites to be used in flexible applications.

Interestingly, the Young's modulus of BTO/CFO free-standing films is much lower than that of bulk BTO (≈120 GPa) and bulk CFO (≈188 GPa).[23–26] Ceramic materials that are brittle and tough in bulk can show abnormal mechanical behavior at the nanoscale, such as ultrahigh- or superelasticity and low Young's modulus.[7,27,28] Unlike bulk materials, surface and interface contributions can be accounted for in the unique tensile mechanical properties of the nanoscale BTO/CFO free-standing structures. In particular, surface stress, originating from surface relaxation and reconstruction, and interface stress, originating from the lattice mismatch, can result in a softening of the elastic moduli and an increase in the maximum elastic strain.[29,30] In addition, the scarcity of internal defects in nanoscale structures compared to bulk materials further restrict dislocation multiplication and crack evolution under tensile stress, resulting in an increase in the elastic limit.[31–33] Furthermore, recent reports about the effect of polarized electric domain rotations on superelasticity can explain the mechanism of flexibility in the BTO/CFO ME composites.[7–9]

We then investigated the ME coupling characteristics in transferred BTO/CFO structures on a PDMS substrate (**Figure 3**a). Transferred BTO/CFO structures showed excellent ME coupling, as shown in Figure 3b,c. Coercive field shifts in piezoelectric force microscopy (PFM) hysteresis loop measurements have been clearly observed with the application of magnetic fields and higher magnetic fields resulted in higher coercive field shifts. As their electrical and magnetic properties highly depend on strain, we also tested their ME coupling behavior while stretching the PDMS substrate. For quantitative analysis, we define the ME coefficient as

$$\alpha_E = \Delta E/\Delta H \quad (1)$$

where ΔH is the applied in-plane magnetic field and ΔE is the measured out-of-plane electric field that can be estimated by the shift of the center of the hysteresis loop.[34] Figure 3d shows ME coupling coefficients as a function of external tensile strain. Although the coercive field shifts and the ME coupling coefficient decreased with larger tensile strain, ME coupling was observed with up to 4.1% of tensile strain (calculated from the deformation of BTO/CFO when PDMS is stretched, Figure S3, Supporting Information). As the applied tensile strain increased from 0% to 4.1%, the coupling coefficient decreased from 16.6×10^5 to 2.04×10^5 mV cm^{-1} Oe^{-1}. In addition, we also tested the repeatability and recoverability of the ME coupling change in transferred BTO/CFO structures by stretching and releasing the PDMS substrate repeatedly. ME coupling coefficients were measured in situ with the strain range from 0% to 3% during stretch-release cycling of the PDMS substrate. As can be seen in Figure 3e, the ME coupling coefficient decreased during stretching, but recovered its values

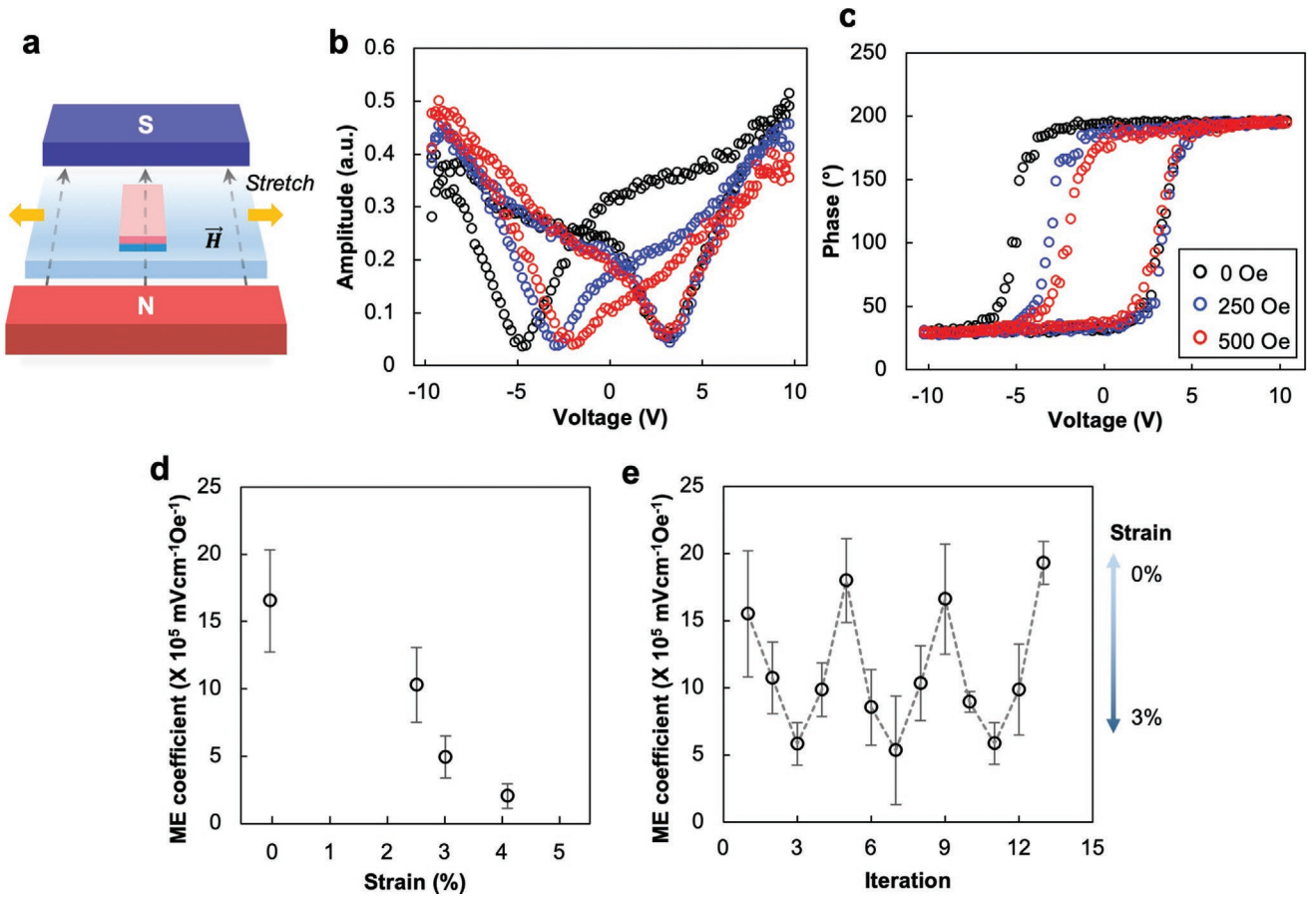

Figure 3. Reversible tuning of ME coupling. a) A schematic illustration of magnetic field application and mechanical stretching directions during PFM measurements. b) Local PFM hysteresis amplitude and c) phase of transferred BTO/CFO structures under magnetic fields. d) ME coupling coefficients as a function of applied tensile strain. e) Reversible tuning of ME coupling in transferred BTO/CFO structures.

when released. This behavior was observed for several cycles, and thus, change of the ME coefficient over strain was repeatable. Delamination was not observed during the repeatability test. For a long-term application, high and durable adhesion between the flexible substrate and ME composite can be ensured by surface treatment.[35]

To analyze the effect of the geometrical configuration on ME coupling behavior, we compared the ME coupling coefficients in BTO/CFO structures of different mechanical boundary conditions, including free-standing structures, stretchable structures on a PDMS substrate, square-disk patterned structures on a rigid substrate, and as-deposited thin films (**Figure 4**). Higher mechanical degrees of freedom in ME composites results in a higher ME coupling coefficient, which can be attributed to the reduced substrate clamping in the BTO/CFO.[21] We also compared our results with other ME nanocomposites evaluated with similar methods, and the ME coefficient of free-standing BTO/CFO composites is among the highest (i.e., $CoFe_2O_4$-$BiFeO_3$ core–shell nanoparticle: 3.25×10^5 mV cm^{-1} Oe^{-1},[36] $CoFe_2O_4$–$Pb(Zr_{0.52}Ti_{0.48})O_3$ core–shell nanofiber: 2.95×10^4 mV cm^{-1} Oe^{-1},[37] $CoFe_2O_4$-$BiFeO_3$ core–shell nanofiber: 2.2–2.5 $\times 10^4$ mV cm^{-1} Oe^{-1},[38] FeGa/P(VDF-TrFE) ferroelectric polymer, 9.4×10^4 mV cm^{-1} Oe^{-1},[39] quasi-(0-3)

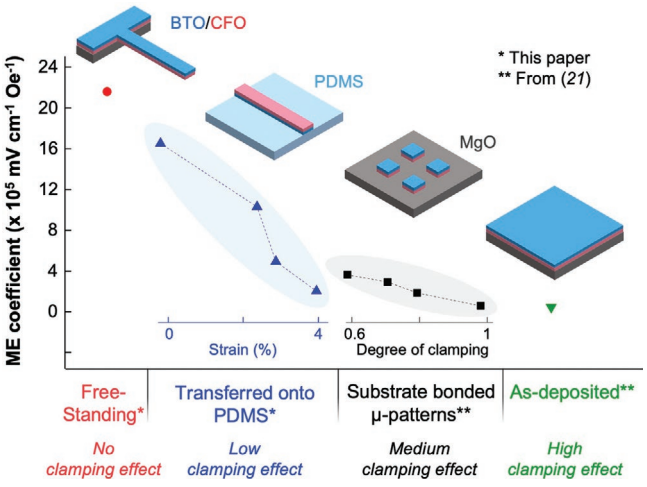

Figure 4. Comparison of the ME coupling coefficients changed by the geometry and configuration of the BTO/CFO thin film. ME coupling coefficients were calculated based on the PFM measurements on free-standing, transferred, patterned, and as-deposited BTO/CFO thin film structures. The data for the micro-patterns (reduced substrate clamping effect) and as-deposited thin films were taken from ref. [21].

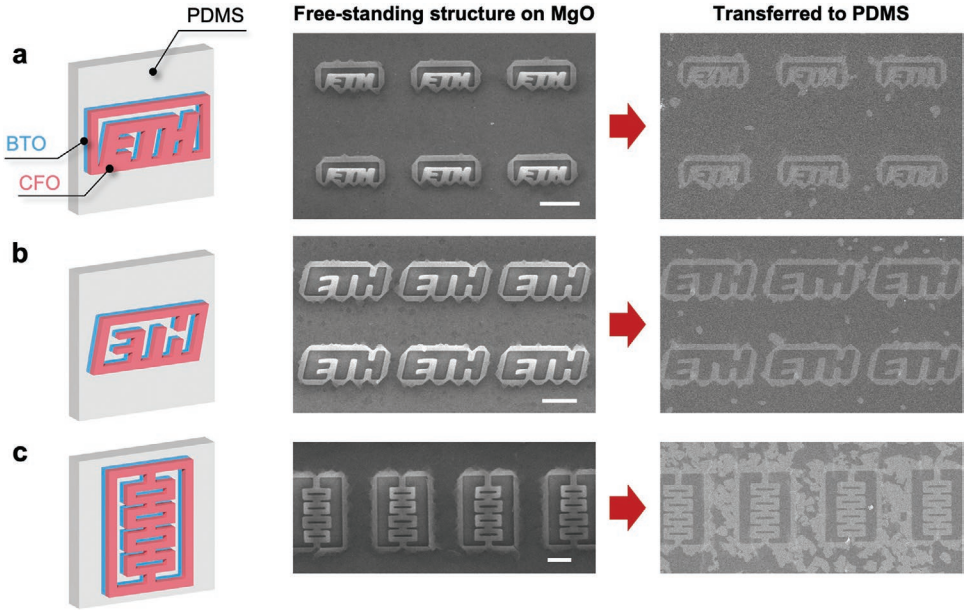

Figure 5. Transfer of various patterns of ME composite. Stamp-transferring of various designs of BTO/CFO free-standing structures including a) positively engraved ETH logo, b) negatively engraved ETH logo, and c) connected rectangular arrays. The scale bars indicate 10 µm.

nanocomposite: 338 mV cm^{-1} Oe^{-1}[40]). This high ME coefficient does not only originate in the reduced clamping but also from preferred crystalline orientation in the epitaxial thin film. Another interesting feature in BTO/CFO stretchable structures on PDMS is real-time tuning of ME coupling coefficient, which otherwise cannot be realized in the patterned thin films on substrates where the ME couplings are fixed once films have been fabricated.[21]

The strain-dependent ME coupling in BTO/CFO on the PDMS substrate can be attributed to three possible factors: i) Tensile strain from the PDMS substrate exerts a 'clamping' effect on the CFO layer, preventing effective magnetostriction and interfacial interaction with BTO, and eventually resulting in weak ME coupling. ii) The magnetostriction of CFO also depends on the external mechanical stress. In a simplified magneto-elastic model which considers unidirectional stress in magnetic materials, the magnetostriction coefficient can be expressed as

$$\lambda = \lambda_{100}\left(1 - \frac{3\left(\exp\left(\frac{3}{2}A_s\lambda_{100}\sigma_{yy}\right)+1\right)}{2\left(\cosh(\kappa H)+\exp\left(\frac{3}{2}A_s\lambda_{100}\sigma_{yy}\right)+1\right)}\right) \quad (2)$$

where

$$A_S = \frac{3\chi^0}{\mu_0 M_S} \quad (3)$$

$$\kappa = \mu_0 A_s M_s \quad (4)$$

μ_0 is the vacuum permittivity, M_s is the saturation magnetization, λ_{100} is the magnetostrictive coefficient, and χ^0 is the initial slope of the unstressed anhysteretic magnetization curve.[41,42] Therefore, the increase in the uniaxial tensile stress σ_{yy} gives rise to a decrease in the magnetostriction λ and eventually a weak ME coupling. iii) Under large tensile strain, BTO shows negligible out-of-plane polarization (P_{op}) as well as weaker strain sensitivity, $\frac{\partial P_{op}}{\partial \varepsilon}$.[43–46] Therefore, diminished ME coupling can be expected under large tensile strain since the magnetostriction of CFO would cause only a small change in P_{op} in BTO.

Our results indicate that ME coupling of transferred BTO/CFO structures can be systematically tuned in real-time by applying different tensile strains via stretching the PDMS substrate, unlike thin films on rigid substrates where external strains are fixed by the lattice parameters of the substrate. The reversibly tunable ME coupling also provides opportunities for BTO/CFO transferred structures to be used for stretchable magnetoelectrics for strain-sensing applications (Figure 3d). In flexible and stretchable magnetoelectrics, the ability to fabricate various shapes and figures on different substrates allows for multiple designs and further expansion of their applications. To this end, the adopted stamp-transfer method is a versatile approach for the realization of BTO/CFO architectures with different sizes and shapes. In **Figure 5**, we show various designs transferred by the stamping method, including positively and negatively engraved ETH alphabet logos and connected-rectangular arrays. From just a few to tens of microns, all the architectures were successfully transferred to a large area substrate without any fracture within the structures, providing uniformity and scalability of transferring BTO/CFO structures using the stamping method.

3. Conclusion

In summary, BTO/CFO free-standing thin films showed exceptionally high elastic tensile strain and ME coupling. BTO/CFO

films transferred to a PDMS substrate exhibited robust, repeatable and recoverable ME coupling behavior under high strains. Tunable ME coupling by stretching (88% decrease in ME coefficient with 4.1% of tensile strain) and its reversibility (cyclic stretch and release between 0% and 3% of strain) were demonstrated. Demonstration of ME coupling showed potential for sensing magnetic fields or giving electric stimulus remotely. It is also possible to tailor the actual strain distribution in the materials and maintain constant ME coupling coefficient even under large stretching by adopting functional pattern designs such as fractals or auxetics. We believe that high-performance flexible ME composites and their capability to be transferred onto stretchable substrates with desired geometries will enable new soft robotics and advanced M/NEMS applications.

4. Experimental Section

Thin Film Deposition and Fabrication: BTO (15 nm)/CFO (15 nm) epitaxial thin films were deposited on (001) oriented MgO single crystalline substrate (Crystal GmbH) using pulsed laser deposition (Figure S4, Supporting Information).[21] A CFO layer was deposited at 550 °C and 10 mTorr oxygen partial pressure with the laser intensity and frequency of 1.8 J cm^{-2} and 5 Hz, respectively. A BTO layer was then deposited at 750 °C and 200 mTorr oxygen partial pressure and the laser parameters of 1.2 J cm^{-2} and 4 Hz. Subsequently, photoresist (AZ 1505) was spin-coated on the BTO/CFO thin films and patterned with different shapes using UV-photolithography. Patterned films were dry-etched with Ar-ion milling (Oxford IonFab 300 Plus) and the remaining photoresist was rinsed off with acetone (5 min), isopropyl alcohol (5 min), and oxygen plasma (600 W, 3 min). Afterward, the MgO substrate was chemically etched with a sodium bicarbonate saturated solution and dried with a critical point dryer (Tousimis-CPD). As a result, various shapes of free-standing BTO/CFO structures were obtained (Figure S5, Supporting Information). Some of these free-standing structures were stamped with a PDMS substrate and were successfully transferred.

Materials Characterization: Piezoelectric properties and ME couplings were measured with piezoresponse force microscopy (PFM, ND-MDT) equipped with an in-plane DC magnetic field setup. A customized sample stage was designed in order to apply uniaxial strains on BTO/CFO//PDMS structures during the PFM measurements (Figure S6, Supporting Information). The BTO/CFO structures were patterned with bridge-like linear stripes of 1 μm width (Figure S5, Supporting Information) and transferred onto the PDMS substrate. During the PFM measurements, mechanical strain was applied vertically to the magnetic field direction (Figure 3a). The strain was estimated by the elongated (stretched) width of the BTO/CFO stripes compared to the as-transferred width (Figure S3, Supporting Information). The ME coupling coefficients were calculated based on the local piezoelectric hysteresis loops averaged over five measurements.

In Situ Nanomechanical Tensile Testing: For the quantitative investigation of the stretchability and the estimation of the maximum mechanical endurance without developing fractures like necks and cracks, the mechanical properties of BTO/CFO free-standing films, specifically failure stress and strain, were evaluated using nanomechanical force sensors. Tensile tests were performed using a scanning electron microscope (Nova NanoSEM 450, FEI company) equipped with a nanomechanical testing system (FT-NMT03, Femtotools AG) at room temperature. A BTO/CFO dogbone-like structure was attached to the tungsten force sensor probe (radius less than 0.1 μm) using SEM-compatible glue (SEMGLU, Kleindiek Nanotechnik GmbH) and the force was measured with 100 Hz sampling frequency under a 5 nm s^{-1} loading rate using a micro-electro-mechanical system-based force sensor (model FT-S200, ± 200 μN force range limit and 0.5 nN resolution). Inspired by the ASTM standard,[22] dogbone-like structures for mechanical tensile fracture tests were designed. These structures were designed to have a narrow neck, where elongation and fractures in the material could take place. Two markers were added along the neck of the dogbone-like structure to analyze the elongation. The elongated lengths and strains of the dogbone-like structures were calculated based on the marker positions. Since the distance between the markers measured from the SEM images were highly dependent on the tilting of the sample, the geometrical configuration, particularly the tilting angle between the beam and the sample, was carefully controlled. First, the initial distance between the two markers of the flat sample was measured (Figure S7, Supporting Information, left). The sample stage was then tilted and the sample was attached to the force sensor. To recover from the stage tilting, the attached sample was raised (Figure S7, Supporting Information, right).

Supporting Information

Supporting Information is available from the Wiley Online Library or from the author.

Acknowledgements

M.K. and D.K. contributed equally to this work. This work was financed by the ERC Consolidator Grant "Highly Integrated Nanoscale Robots for Targeted Delivery to the Central Nervous System" HINBOTS under grant no. 771565, the MSCA-ITN training program "mCBEEs" under grant no. 764977, the ERC Advanced Grant "Soft Micro Robotics" SOMBOT under grant no. 743217, and the Swiss National Science Foundation (Project No. 200021L_192012). X.-Z.C. would like to acknowledge the Swiss National Science Foundation (No. CRSK-2_190451) for partial financial support. M.K. acknowledges partial financial support from the Swiss National Science Foundation under Project No. 200021L_197017. H.C. acknowledges the National Research Foundation of Korea (2021M3F7A1082275 and 2017K1A1A2013237). J.P.-L. acknowledges funding from the Swiss National Science Foundation, Project No. 200021_181988 and grant PID2020-116612RB-C33 funded by MCIN/AEI /10.13039/501100011033. The authors would also like to thank the Scientific Center for Optical and Electron Microscopy (ScopeM), the FIRST laboratory at ETH for their technical support, and the Cleanroom Operations Team of the Binning and Rohrer Nanotechnology Center (BRNC) for their help and support. The authors have a consent from the ETH Kommunikationsberatung Team to use the logo of ETH Zürich in Figure 5.

Open access funding provided by Eidgenossische Technische Hochschule Zurich.

Conflict of Interest

The authors declare no conflict of interest.

Data Availability Statement

The data that support the findings of this study are available from the corresponding author upon reasonable request.

Keywords

magnetoelectric, micro-/nanoelectromechanical system, multiferroics, soft robotics, thin film

Received: December 9, 2022
Revised: January 30, 2023
Published online: February 28, 2023

[1] P. Wang, M. Hu, H. Wang, Z. Chen, Y. Feng, J. Wang, W. Ling, Y. Huang, *Adv. Sci.* **2020**, *7*, 2001116.
[2] B. D. Gates, *Science* **2009**, *323*, 1566.
[3] F. Hartmann, M. Baumgartner, M. Kaltenbrunner, *Adv. Mater.* **2021**, *33*, 2004413.
[4] C. Laschi, B. Mazzolai, M. Cianchetti, *Sci. Rob.* **2016**, *1*, eaah3690.
[5] K. S. Ramadan, D. Sameoto, S. Evoy, *Smart Mater. Struct.* **2014**, *23*, 033001.
[6] D. Berlincourt, H. Jaffe, *Phys. Rev.* **1958**, *111*, 143.
[7] G. Dong, S. Li, M. Yao, Z. Zhou, Y.-Q. Zhang, X. Han, Z. Luo, J. Yao, B. Peng, Z. Hu, H. Huang, T. Jia, J. Li, W. Ren, Z.-G. Ye, X. Ding, J. Sun, C.-W. Nan, L.-Q. Chen, J. Li, M. Liu, *Science* **2019**, *366*, 475.
[8] H. Elangovan, M. Barzilay, S. Seremi, N. Cohen, Y. Jiang, L. W. Martin, Y. Ivry, *ACS Nano* **2020**, *14*, 5053.
[9] D. Kim, M. Kim, S. Reidt, H. Han, H. Choi, J. Puigmartí-Luis, M. Trassin, B. J. Nelson, X.-Z. Chen, S. Pané, *Nat. Commun.*, https://doi.org/10.1038/s41467-023-36274-w.
[10] G. Dong, Y. Hu, C. Guo, H. Wu, H. Liu, R. Peng, D. Xian, Q. Mao, Y. Dong, Y. Zhao, B. Peng, Z. Wang, Z. Hu, J. Zhang, X. Wang, J. Hong, Z. Luo, W. Ren, Z.-G. Ye, Z. Jiang, Z. Zhou, H. Huang, Y. Peng, M. Liu, *Adv. Mater.* **2022**, *34*, 2108419.
[11] S. H. Seung, M. Gu, M. Verma, V. Harbola, Y. W. Bai, D. Lu, A. Vailionis, Y. Hikita, R. Pentcheva, M. R. James, Y. H. Harold, *Science* **2020**, *368*, 71.
[12] R. Xu, J. Huang, E. S. Barnard, S. S. Hong, P. Singh, E. K. Wong, T. Jansen, V. Harbola, J. Xiao, B. Y. Wang, S. Crossley, D. Lu, S. Liu, H. Y. Hwang, *Nat. Commun.* **2020**, *11*, 3141.
[13] D. Pesquera, A. Fernández, E. Khestanova, L. W. Martin, *J. Phys.: Condens. Matter* **2022**, *34*, 383001.
[14] D. Pesquera, E. Parsonnet, A. Qualls, R. Xu, A. J. Gubser, J. Kim, Y. Jiang, G. Velarde, Y.-L. Huang, H. Y. Hwang, R. Ramesh, L. W. Martin, *Adv. Mater.* **2020**, *32*, 2003780.
[15] N. A. Spaldin, R. Ramesh, *Nat. Mater.* **2019**, *18*, 203.
[16] X. Liang, H. Chen, N. X. Sun, *APL Mater.* **2021**, *9*, 041114.
[17] N. Ortega, A. Kumar, J. F. Scott, R. S. Katiyar, *J. Phys.: Condens. Matter* **2015**, *27*, 504002.
[18] J.-M. Hu, C.-W. Nan, *APL Mater.* **2019**, *7*, 080905.
[19] R. Wu, J. L. MacManus-Driscoll, *APL Mater.* **2022**, *10*, 010901.
[20] S. Kopyl, R. Surmenev, M. Surmeneva, Y. Fetisov, A. Kholkin, *Mater. Today Bio* **2021**, *12*, 100149.
[21] D. Kim, M. D. Rossell, M. Campanini, R. Erni, J. Puigmartí-Luis, X.-Z. Chen, S. Pané, *Appl. Phys. Lett.* **2021**, *119*, 012901.
[22] ASTM International Committee E-28 on Mechanical Testing, in *Standard test Methods for Tension Testing of Metallic Materials*, ASTM international, West Conshohocken, PA, USA **2022**.
[23] A. C. Dent, C. R. Bowen, R. Stevens, M. G. Cain, M. Stewart, *J. Eur. Ceram. Soc.* **2007**, *27*, 3739.
[24] N. M. Aimon, J. Liao, C. A. Ross, *Appl. Phys. Lett.* **2012**, *101*, 232901.
[25] T. Tanimoto, K. Okazaki, K. Yamamoto, *Jpn. J. Appl. Phys.* **1993**, *32*, 4233.
[26] O. Viun, F. Labesse-Jied, R. Moutou-Pitti, V. Loboda, Y. Lapusta, *Acta Mech.* **2015**, *226*, 2225.
[27] A. Lai, Z. Du, L. G. Chee, A. S. Christopher, *Science* **2013**, *341*, 1505.
[28] C. Dang, J.-P. Chou, B. Dai, C.-T. Chou, Y. Yang, R. Fan, W. Lin, F. Meng, A. Hu, J. Zhu, J. Han, M. M. Andrew, J. Li, Y. Lu, *Science* **2021**, *371*, 76.
[29] R. C. Cammarata, *Prog. Surf. Sci.* **1994**, *46*, 1.
[30] S. Wang, Z. Shan, H. Huang, *Adv. Sci.* **2017**, *4*, 1600332.
[31] A. Banerjee, D. Bernoulli, H. Zhang, M.-F. Yuen, J. Liu, J. Dong, F. Ding, J. Lu, M. Dao, W. Zhang, Y. Lu, S. Suresh, *Science* **2018**, *360*, 300.
[32] T. Zhu, J. Li, *Prog. Mater. Sci.* **2010**, *55*, 710.
[33] C. J. Shih, M. A. Meyers, V. F. Nesterenko, S. J. Chen, *Acta Mater.* **2000**, *48*, 2399.
[34] H. Miao, X. Zhou, S. Dong, H. Luo, F. Li, *Nanoscale* **2014**, *6*, 8515.
[35] S. Yao, Y. Zhu, *Adv. Mater.* **2015**, *27*, 1480.
[36] D. Kim, I. Efe, H. Torlakcik, A. Terzopoulou, A. Veciana, E. Siringil, F. Mushtaq, C. Franco, D. von Arx, S. Sevim, *Adv. Mater.* **2022**, *34*, 2110612.
[37] S. Xie, F. Ma, Y. Liu, J. Li, *Nanoscale* **2011**, *3*, 3152.
[38] Q. Zhu, Y. Xie, J. Zhang, Y. Liu, Q. Zhan, H. Miao, S. Xie, *J. Mater. Res.* **2014**, *29*, 657.
[39] X. Z. Chen, M. Hoop, N. Shamsudhin, T. Huang, B. Özkale, Q. Li, E. Siringil, F. Mushtaq, L. Di Tizio, B. J. Nelson, *Adv. Mater.* **2017**, *29*, 1605458.
[40] Y. Li, Z. Wang, J. Yao, T. Yang, Z. Wang, J.-M. Hu, C. Chen, R. Sun, Z. Tian, J. Li, *Nat. Commun.* **2015**, *6*, 1.
[41] L. Daniel, M. Rekik, O. Hubert, *Arch. Appl. Mech.* **2014**, *84*, 1307.
[42] L. Daniel, *Eur. Phys. J.: Appl. Phys.* **2018**, *83*, 30904.
[43] P. V. Ong, J. Lee, *J. Appl. Phys.* **2012**, *112*, 014109.
[44] C. Ederer, N. A. Spaldin, *Phys. Rev. Lett.* **2005**, *95*, 257601.
[45] J. Wang, Y. Xia, L.-Q. Chen, S.-Q. Shi, *J. Appl. Phys.* **2011**, *110*, 114111.
[46] S. Choudhury, Y. L. Li, L. Q. Chen, Q. X. Jia, *Appl. Phys. Lett.* **2008**, *92*, 142907.